Modeling Of Vacancy Cluster Formation In Ion Implanted Silicon

Srinivasan Chakravarthi[†] and Scott T. Dunham[‡]

[†]Department of Manufacturing Engineering, Boston University, Boston, MA 02215.
(Current affiliation: Silicon Technology Development, Texas Instruments, Dallas, TX 75265)
[‡]Department of Electrical Engineering, University of Washington, Seattle, WA 98195.

Ion implantation of silicon introduces excess point defects that quickly recombine during annealing leaving net interstitial and vacancy populations. For higher energy implants, the separation between interstitials and vacancies is larger, leading to a vacancy rich region towards the surface and an interstitial rich region deeper in the bulk. The high supersaturation of vacancies in the near surface region can lead to their aggregation into vacancy clusters or voids. In this work, we have developed a continuum model for vacancy clusters using discrete cluster sizes. Results from atomistic calculations [1] are used for the energetics of the cluster growth/dissolution. The model is compared to data from Venezia *et al.* [2] for Au indiffusion subsequent to Si high energy implants. We found good agreement with experimental data using this model without any tuning of the parameters. However, this model is too complex and computationally expensive to be effectively incorporated into continuum TCAD solvers. Hence, we reduced this system of discrete rate equations into a two-moment model by carefully considering the behavior of the full model under a range of conditions. The parameters of the moment-based model follows from the full model, which in turn is based on atomistic calculations. The resulting simple and computationally efficient model is found to accurately reproduce the Au labelling experiments.

1. Introduction

Modeling the annealing of an ion-implanted silicon is a complicated process. Large numbers of point defects are created during the implant, and these can coalesce to form various extended defects. Recent experimental observations suggest that the annealing process for low/medium energy implants is independent of the initial implant cascade and mainly dependent on the distribution of the implanted ion.[3,4] This is because implantation creates large but nearly equal numbers of interstitials and vacancies that quickly recombine, leaving behind the introduced extra ion-interstitial. However, it is possible to achieve a larger separation between interstitial and vacancy distributions after the implant cascade via high energy implantation which kicks interstitials deeper into the bulk. In this case, recombination leaves a substantial vacancy rich region near the surface.

Several experiments have indicated the presence of this vacancy rich region. Enhanced diffusion of Sb marker layers have been observed after MeV Si implants.[5] For high energy implants, metallic impurities getter not only at R_p, the projected range of the implant but also at $R_p/2$.[6] The gettering at R_p is attributed to interstitial type defects, whereas the gettering at $R_p/2$ is explained by the presence of the excess vacancies from the implant. It is also possible to create a vacancy rich region by higher mass implants. Pb implants have been found to decrease boron clustering in shallow boron marker layers.[7] This vacancy rich layer can be used as a tool to reduce the depth and increase activation of boron or phosphorus junctions. For instance, use of MeV Si implants have been found to reduce the interstitials in end of range loops from high dose implants.[8] Similarly, use of higher energy sub-amorphizing Si implants have been found to reduce transient enhanced diffusion (TED) for medium dose boron implants.[9]

Since the vacancy induced effects seem to last over a significant annealing time,[5] vacancies most likely agglomerate into vacancy clusters or voids. Understanding and modeling vacancy clusters is thus essential

to modeling diffusion following well formation and exploring the novel use of vacancies in the formation of next generation devices. In this work, we model the formation and subsequent annealing of this vacancy rich layer.

2.   Model

Bongiorno *et al.* performed tight binding molecular dynamics (TBMD) calculations to obtain formation and binding energies for vacancy clusters in silicon for $n \leq 35$.[1] Their results show that different growth patterns for cluster formation exist. The binding energy $E_b(n)$ for adding a vacancy to a $n - 1$ size cluster is not a smooth function of size. For small clusters ($n < 24$), Hexagonal Ring Clusters (HRC, clusters grown by removing Si atoms from the 6-membered rings present in the Si crystal structure) are energetically favorable with respect to Spheroidal Clusters (SPC, clusters grown by removing Si atoms from successive shells of neighbors surrounding a given atom). Hence, we use calculated values for SPC for larger clusters and HRC for smaller clusters. In the absence of TBMD calculations for clusters larger than 35, we use a functional form for the binding energy from Jaraiz *et al.*[10]

In our analysis, discrete reactions are solved at each cluster size. Clusters can grow or dissolve with addition or release of a vacancy,

$$V_{n-1} + V \Leftrightarrow V_n. \tag{1}$$

Vacancy clusters can also interact with interstitials,

$$V_n + I \Leftrightarrow V_{n-1}. \tag{2}$$

The net rate of formation of size n cluster from size $n - 1$ is given by the difference of the rates of Eqs. 1 and 2 as:

$$I_{V_n} = I_{V_n}^{V/V_{n-1}} - I_{V_n}^{I/V_n}. \tag{3}$$

We assume vacancy incorporation reaction kinetics are diffusion limited, and hence the rate of formation $I_{V_n}^{V/V_{n-1}}$ of V_n from Eq. 1 is given by,

$$I_{V_n}^{V/V_{n-1}} = \sigma_{n-1}^{V/V_{n-1}} D_V \left(C_{V_{n-1}} C_V - \frac{C_{V_n}}{K_{V_n}^{V/V_{n-1}}} \right), \tag{4}$$

where D_V is the vacancy diffusivity and $\sigma_{n-1}^{V/V_{n-1}}$ is the capture radius of the reaction and is defined as

$$\sigma_n^{V/V_{n-1}} = \frac{A_{cap}^{V/V_{n-1}}}{a_{hop}}. \tag{5}$$

a_{hop} is the hop distance and is taken to be equal to a_0, the lattice constant of silicon. A_{cap}^n is the capture cross-section and is given by,

$$A_{cap}^{V/V_{n-1}} = 4\pi (r_{cap}^{V/V_{n-1}})^2 = 4\pi (n - 1)^{2/3} a_0^2. \tag{6}$$

$K_{V_n}^{V/V_{n-1}}$ is the equilibrium constant for Eq. 1 and is given as,

$$K_{V_n}^{V/V_{n-1}} = \left(\frac{1}{5 \times 10^{22} \text{ cm}^{-3}} \right) \exp \left[\frac{E_b(n)}{kT} \right] \tag{7}$$

Table 1: Point defect parameters used for the simulations. (a) Ref. 10, (b) Ref. 12, (c) Ref. 13, (d) Ref. 14.

Parameter	Pre-exponent	Energy (eV)	Ref.
$D_V(\mathrm{cm}^2/s)$	1×10^{-3}	0.43	(a)
$D_V C_V^*(\mathrm{cm}^{-1}\mathrm{s}^{-1})$	6.95×10^{21}	3.88	(b)
$D_I(\mathrm{cm}^2/s)$	0.158	1.37	(c)
$D_I C_I^*(\mathrm{cm}^{-1}\mathrm{s}^{-1})$	1.5×10^{26}	4.95	(d)

The reaction rate for Eq. 2 is given as,

$$I_{V_n}^{I/V_n} = \sigma_n^{I/V_n} D_I \left(C_{V_n} C_I - \frac{C_{V_{n-1}}}{K_{V_n}^{I/V_n}} \right). \tag{8}$$

The equilibrium constant for this reaction can be obtained as,

$$K_{V_{n-1}}^{I/V_n} = \frac{1}{K_{V_n}^{V/V_{n-1}} C_I^* C_V^*}. \tag{9}$$

We assume a small barrier $E_{I/V}$ of 0.2 eV to I/V recombination[11] and hence

$$\sigma_n^{I/V_n} = \frac{A_{cap}^{I/V_n}}{a_{hop}} \exp\left[-\frac{E_{I/V}}{kT}\right] \tag{10}$$

$$= 4\pi(n)^{2/3} a_0 \exp\left[-\frac{E_{I/V}}{kT}\right]. \tag{11}$$

The point defect parameters used in this work are tabulated in Table 1.[10,12,13,14] The vacancy cluster energies from Bongiorno et al.[1] are shown in Table 2. For larger vacancy clusters, the binding energy used from Jaraiz et al.[10] is

$$E_b(n) = 3.65 - 5.15 \left[n^{(2/3)} - (n-1)^{(2/3)} \right]. \tag{12}$$

Net I$-$V and net V$-$I concentrations from TRIM[15] are used as initial conditions. The net I$-$V concentration is defined as $\max(C_I - C_V, 0)$, and similarly, the net V$-$I concentration is $\max(C_V - C_I, 0)$. At the start of simulations, these concentrations are added to the equilibrium interstitial and vacancy concentrations, respectively. We use an analytical model for interstitial type extended defects from previous work by Gencer et al.[16,17,18,19] As per this model, interstitials agglomerate into {311} defects and further transform into loops. The {311} and loop models are calibrated to transmission electron microscopy (TEM) data.[20,21]

3. Initial Damage

Fig. 1 shows a typical set of defect and dopant profiles from TRIM,[15] a Monte Carlo ion implantation simulator. As discussed earlier, the large initial interstitial and vacancy profiles are nearly equal. Subtracting them reveals that the surface is vacancy rich while interstitials are kicked deeper into the substrate. For the implant energy of 40 keV Si, the separation between vacancies and intersitials is low. Close proximity to the surface leads to rapid annihilation of the excess vacancies. Hence this agrees with

Table 2: Parameters from Bongiorno *et al.* (Ref. 1) used for the simulations. $E_f(n)$ is the formation energy and $E_b(n)$ is the binding energy in eV. We use SPC formation energies for $n > 24$ and HRC for the clusters smaller than 25.

Size	1	2	3	4	5	6	7	8	9
$E_f(n)$	3.40	5.20	7.14	9.36	10.68	11.37	13.7	14.08	14.72
$E_b(n)$	-	1.60	1.46	1.18	2.08	2.71	1.07	3.02	2.76

Size	10	11	12	13	14	15	16	17	18
$E_f(n)$	15.58	17.84	18.27	18.86	19.61	22.03	22.44	23.05	23.79
$E_b(n)$	2.54	1.14	2.97	2.81	2.65	0.98	2.99	2.79	2.66

Size	19	20	21	22	23	24	25	26	27
$E_f(n)$	25.27	26.31	26.91	28.36	29.86	30.06	30.71	31.04	31.38
$E_b(n)$	1.92	2.36	2.80	1.95	1.90	3.20	2.75	3.07	3.06

Size	28	29	30	31	32	33	34	35
$E_f(n)$	31.51	31.87	32.67	33.45	34.22	35.00	36.12	36.4
$E_b(n)$	3.27	3.04	2.6	2.62	2.63	2.62	2.28	3.12

the fact that no visible enhancements have been observed for Sb under such conditions.[22] For a high energy implants, the situation is much different. As seen in Fig. 2, there is a distinct net vacancy rich region for a 2 MeV Si implant. The vacancy rich region extends well over 1μm and has net vacancy concentrations on the order of 10^{18} cm^{-3}. This huge vacancy supersaturation can lead to the formation of vacancy type clusters.

4. Comparison To Experiments

One of the primary problems associated with modeling vacancy clusters is the difficulty in directly observing the defects. Most of the available experiments provide indirect evidence of the presence of vacancy clusters. In this paper, we use Au in-diffusion data from Venezia *et al.*[2] for MeV Si implants. In the experiments considered, Si was implanted to a dose of 10^{16}cm^{-2} at different MeV energies. The implants were performed at 300°C to promote recombination of point defects and thus avoid amorphization. Following implantation, the samples were annealed at various temperatures. They were then implanted with Au and annealed at a lower temperature (750°C). Au from the implant was found to getter around $R_p/2$ and was measured by RBS. The final Au concentration was reported to be relatively insensitive to the time of Au drive-in diffusion and is much higher than its equilibrium solubility in silicon. TEM images reveal Au related precipitates approximately 150 Å in diameter distributed over a depth similar to that indicated by the RBS profiles.

Au diffuses rapidly in Si via an interstitial mechanism. Hence, an increase in vacancy concentration moves Au$_i$ more strongly onto substitutional sites, either via Au$_i + V \rightarrow$ Au$_s$ or by decoration of vacancy clusters or voids. The total Au concentration is dependent on the interaction of the Au$_i$ with vacancies and vacancy clusters. A recent study, based on controlled injection of interstitials into the vacancy layer indicates the ratio of Au to vacancies to be closer to unity.[23]

Simulations show that vacancy clusters are fairly stable in the vacancy rich layer and can lead to enhancement of vacancy diffusers like Sb. For example, we obtain a time averaged vacancy supersaturation
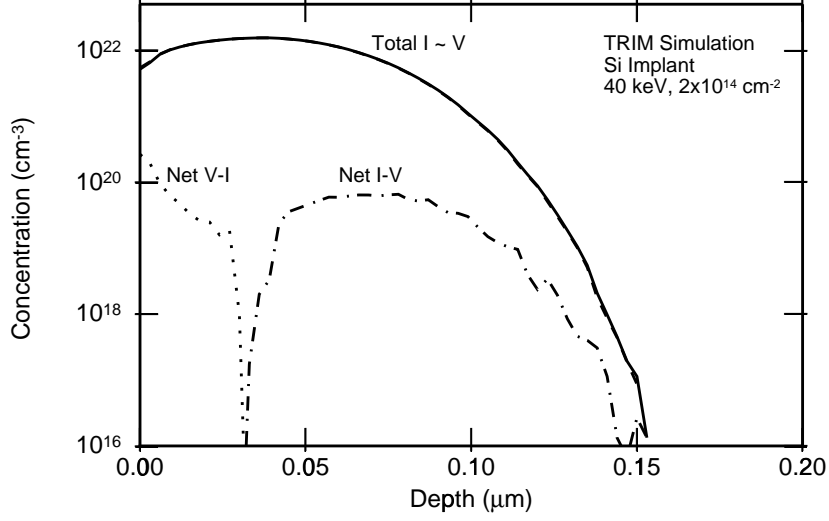
Fig. 1: Monte Carlo simulation showing initial distributions of interstitials and vacancies following a 40 keV, 2×10^{14} cm^{-2} Si implant. Note that in this case the vacancy rich region is close to the surface and hence can be quickly annihilated.

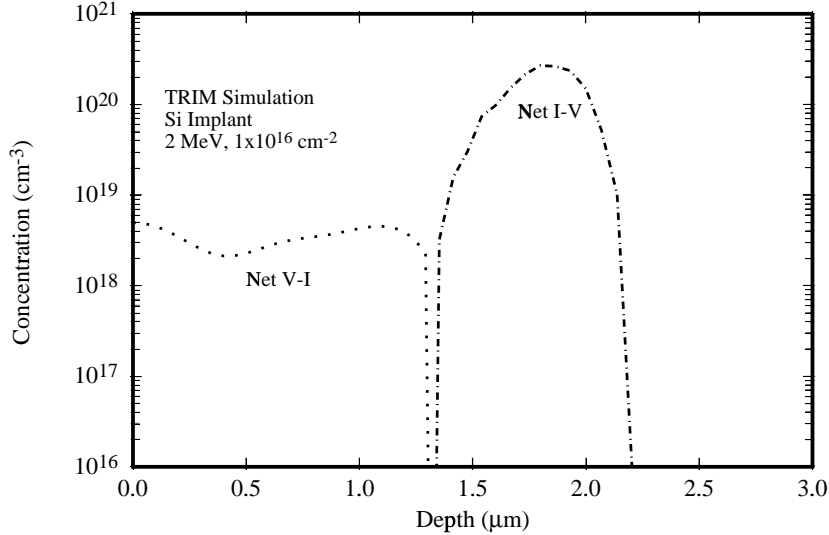**Fig. 2:** Monte Carlo simulation showing net initial distributions of interstitials and vacancies following a 2 MeV, 1×10^{16} cm^{-2} Si implant. The vacancy rich layer extends well over a μm.
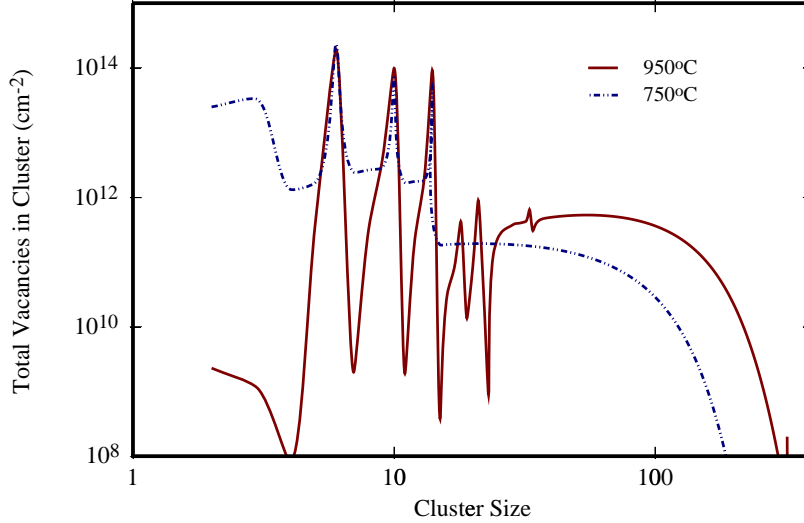
Fig. 3: Simulated size distribution of vacancy clusters after short time anneals at 750°C and 950°C. The distributions are integrated over depth into the silicon. Clusters ripen into larger clusters more predominantly at the higher temperature. This also shows the most stable small cluster sizes to be around 6, 10, 14, 18 and 24.

$(< C_{\mathrm{V}}/C_{\mathrm{V}}^* >)$ of approximately 20 after a 950°C/600 s anneal of a 2 MeV 10^{16} cm^{-2} Si implant. Fig. 3 shows a typical size distribution after a short time anneal at 750°C. As shown here, the most stable clusters are of cluster sizes $n = 6$, 10, 14, 18 and 24. Also shown in the same plot is the distribution at 950°C. It is clear that larger clusters play a more important role at higher temperatures for which there is a rapid growth to larger sizes.

Fig. 4 shows predicted depth profiles for vacancies in clusters compared to observed Au distributions [2] for a 2 MeV 10^{16} cm^{-2} Si implant annealed at 750°C. We obtain a very good match to the experimental data. At 750°C, the clusters are very stable and almost no change in total clustered vacancy concentration is seen between 10 min and 1 h anneals.[2] Fig. 5 shows comparisons to data at 950°C. Note that the simulations again agree well with the time dependence of the data.

One might note that in Figs. 4 and 5, the experiments indicate significant Au concentration down to 1.5μm, in contrast to the simulations for which the clustered V concentration drops off at about 1.2μm. This discrepancy may be due to neglecting channeling in the implant profiles. In the simulated as-implanted profiles, the transition from vacancy-rich to interstitial-rich occurs at about 1.3μm(Fig. 2). Including channeling would extend this crossover deeper into the silicon, giving corresponding deeper V cluster distributions after annealing.

At higher temperatures, vacancy clusters are annihilated by an increased dissolution of interstitial defects from the bulk and surface annihilation of vacancies. Shown in Fig. 6 is the comparison to 1000°C data. The clusters around R$_p$/2 are the largest and therefore the most stable. Hence there is a peak in cluster concentration at R$_p$/2 in the simulations similar to that observed in the experimental data.[2]

We can further analyze our results to see the fraction of vacancies in smaller sized clusters ($n < 36$). Note that these were the clusters for which we used TBMD results from Bongiorno *et al*.[1] Fig. 7 shows the significance of the addition of larger sized clusters. At 750°C, a significant fraction of smaller sized clusters are present. However, at 950°C most of the clusters, especially around R$_p$/2, have ripened into larger clusters ($n > 35$).
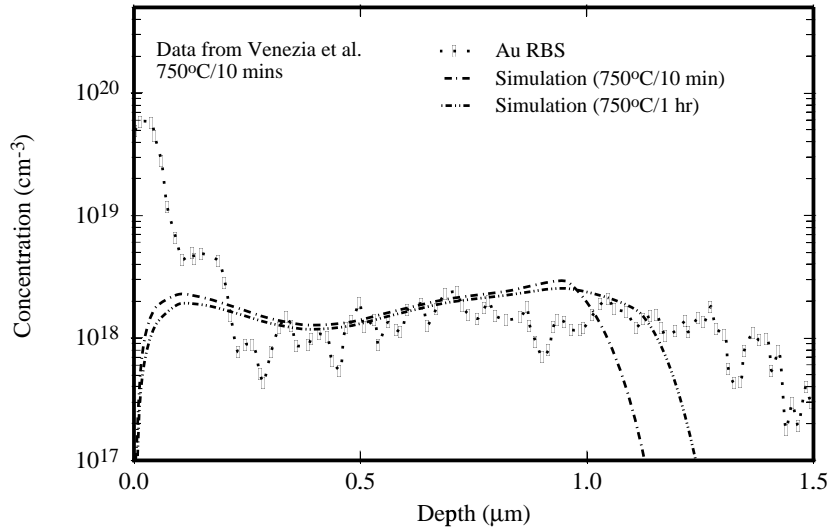
Fig. 4: Simulated clustered vacancy concentrations compared to Au RBS data for 750°C anneals of 10 min and 1 h. Simulations show that there is very little change in the clustered vacancy concentration between 10 min and 1 h. This is in agreement with results from Venezia *et al.* (Ref. 2) who also report that Au concentrations are nearly constant for longer anneals up to 8 h at 750°C. Note that the surface peak in the data is because of the Au implant used for the in-diffusion.
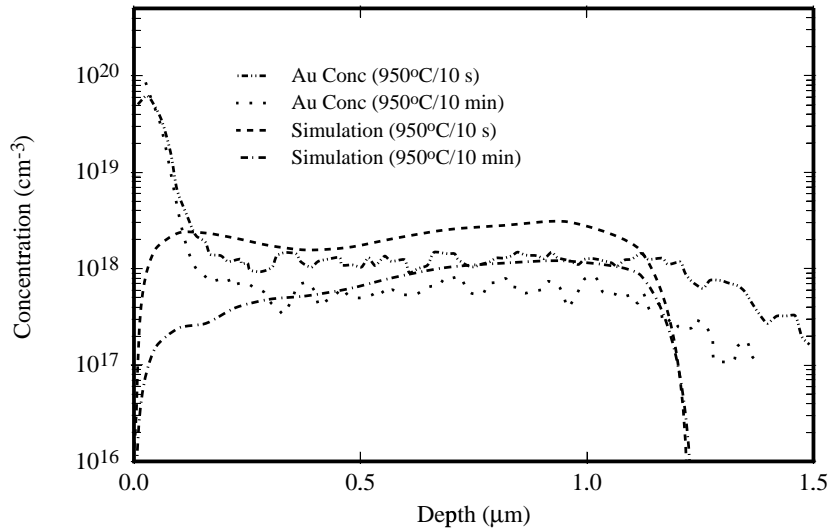

Fig. 5: Simulated and clustered vacancy concentrations compared to Au RBS data after 950°C anneal of 10 s and 10 min. At 950°C, vacancy clusters are annihilated by an increased dissolution of interstitial defects from the bulk and loss to the surface. Note that the simulations agree well with the time dependence of the data. Experimental Au concentration data is from Venezia *et al.* (Ref. 2).
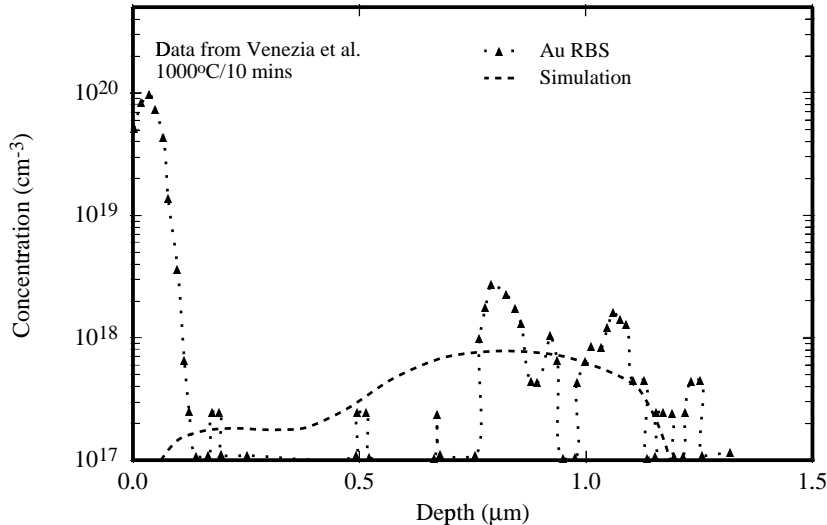
Fig. 6: Simulation and clustered vacancy concentrations compared to Au RBS data after a 1000°C anneal of 10 min. At 1000°C, the vacancy clusters are increasingly annihilated from the surface and the dissolution of interstitial defects from the bulk. The clusters around $R_p/2$ are the largest and therefore the most stable. Hence there is a peak in cluster concentration at $R_p/2$ (0.9 μm) in the simulations similar to that observed in the experimental data. Experimental Au concentration data is from Venezia *et al.* (Ref. 2).

An important factor in matching the vacancy clustering is related to the interstitial clustering model used. Since these simulations involve a deep, high dose of implant, we can expect to see considerable transformation to loops. Indeed, in all the simulations most of the {311} defects transform into loops. If we use only a {311} model and do not consider loop formation, the vacancy clusters are quickly annihilated by the interstitials from the bulk at the higher temperatures. As seen in Fig. 8, using only a {311} model without any loop formation leads to dissolution of all the clusters in a time span of less than 60 s at 950°C, contrary to the experimental observations.

5. Moment Based Models

The physical rate equation model described in the previous sections is computationally very expensive since the full size distribution is tracked at each point in space. Even if one limits the number of precipitate sizes that will be solved for via rediscretization, the number of variables is still very large for efficient solution of the equation system. If the system has multiple spatial dimensions, the number of solution variables becomes prohibitively large. Clejan *et al.* developed a more efficient approach based on considering the size distribution in terms of a small number of moments.[24] Only the evolution of those moments are considered rather than the full distribution at each point in space. The moments are defined as: [24]

$$m_i = \sum_{n=2}^{\infty} n^i f_n, \tag{13}$$

where $i = 0, 1, 2, \ldots$. The zeroth order moment of the distribution is simply the precipitate density, while the first moment corresponds to the density of precipitated solute atoms. Higher order moments further describe the shape of the size distribution. Differentiating Eq. 13 leads to the following system
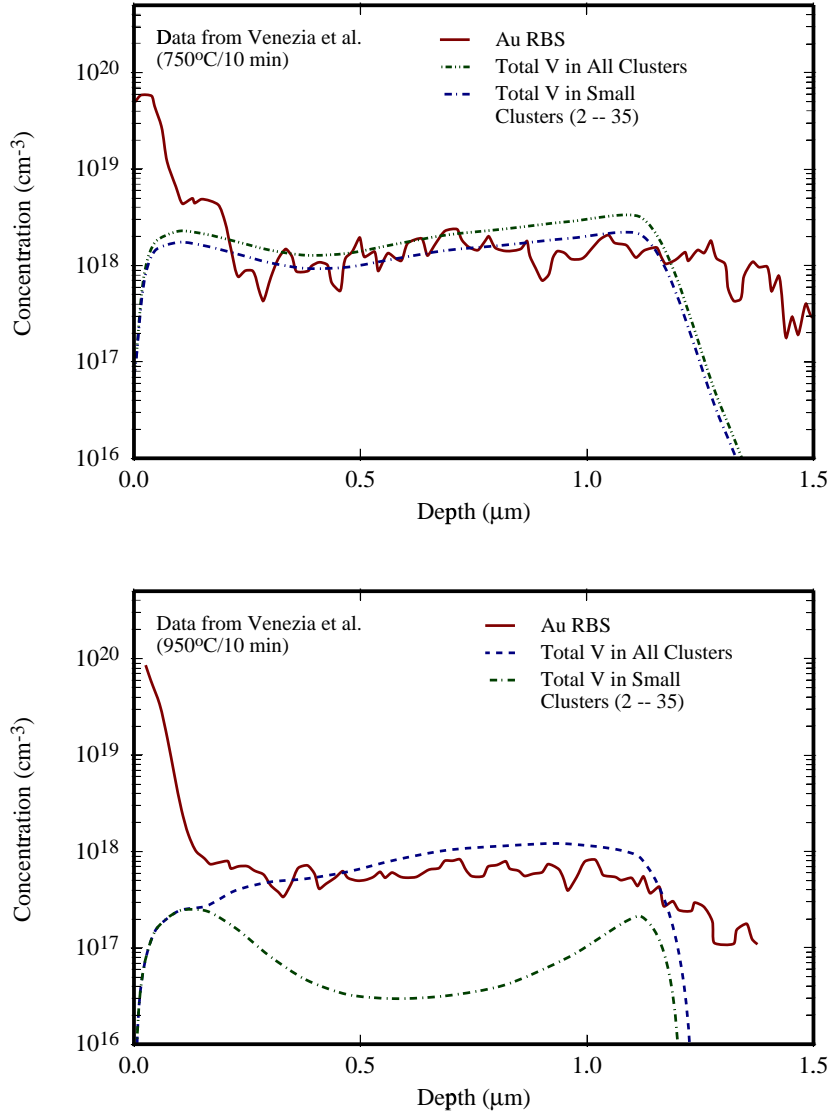
Fig. 7: The above figure shows the significance of the addition of larger sized clusters. At 750°C, smaller sized clusters dominate. However, at 950°C most of the clusters especially around $R_p/2$ have ripened into larger clusters ($n > 35$). Experimental data is from Venezia *et al.* (Ref. 2).
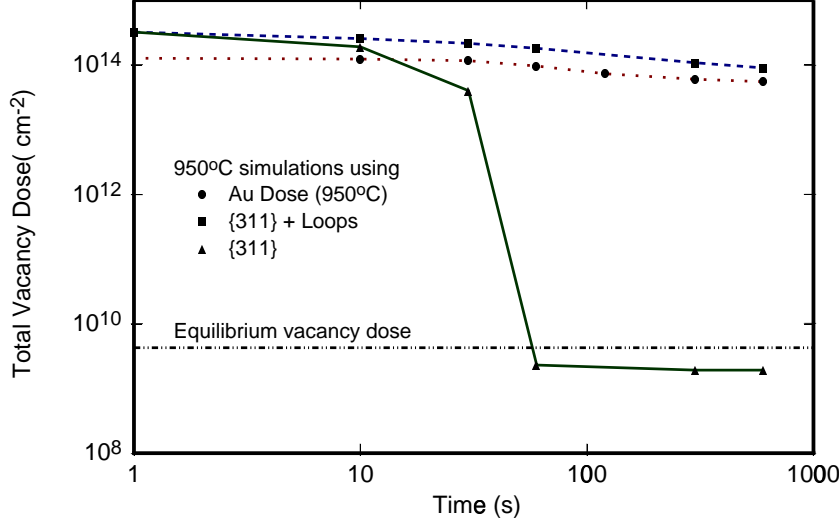
Fig. 8: Time dependence of vacancies in system (depth of 1000 μm). Using only a {311} model without any loop formation leads to dissolution of all the clusters by about 60 s, contrary to experiments. It should be noted that the experimental value reported by Venezia *et al.* is measured between $0.2 - 1$ μm to avoid including the Au implant profile. This method thus leaves out the dose of vacancies below 0.2 μm. Hence the experimental results are expected to be slightly lower than the simulation results despite having a good agreement in the depth distributions. Also, without loops the vacancy concentration drops below the equilibrium value due to the interstitial supersaturation from the dissolving {311} defects. Experimental data is from Venezia *et al.* (Ref. 2).

of equations: [24]

$$\frac{\partial m_i}{\partial t} = 2^i I_1 + \sum_{n=2}^{\infty} \left[(n+1)^i - n^i \right] I_n \tag{14}$$

where, I_n is $I_{V_{n+1}}^{V/V_n}$ as given in Eq. 4. Note that the sums over the I_n can all be written in terms of sums over f_n, nf_n, etc. Hence, they can be calculated from the moments if the finite number of moments considered are sufficient to describe the size distribution. This reduces the system of equations to be solved to: [18]

$$
\begin{aligned}
\frac{\partial m_i}{\partial t} &= D_{\mathrm{V}} \left[2^i \lambda_1 C_{\mathrm{V}}^2 + m_0 C_{\mathrm{V}} \gamma_i^+ - m_0 C_{\mathrm{ss}} \gamma_i^- \right] \\
\gamma_i^+ &= \sum_{n=2}^{\infty} \left[(n+1)^i - n^i \right] \lambda_n \hat{f}_n \\
\gamma_i^- &= \lambda_1 \hat{C}_1^* \hat{f}_2 + \sum_{n=2}^{\infty} \left[n^i - (n-1)^i \right] \lambda_{n-1} \hat{C}_{n-1}^* \hat{f}_n
\end{aligned}
\tag{15}
$$

where $\hat{C}_n^* = C_n^*/C_{\mathrm{ss}}$ and $\hat{f}_n = f_n/m_0$.

If we allow interstitials react with the vacancy clusters, we need to add extra terms to the moment equations. With the same definitions of γ_i as before and setting $\bar{\gamma}_0 = \lambda_2 \hat{f}_2$, the moments can be derived to be: [18]

$$\frac{\partial m_0}{\partial t} = D_{\mathrm{V}} \left[\lambda_1 C_{\mathrm{V}}^2 - m_0 C_{\mathrm{ss}} \gamma_0 \right] - D_{\mathrm{I}} C_{\mathrm{I}} m_0 \bar{\gamma}_0$$

$$\frac{\partial m_1}{\partial t} = D_V \left[2\lambda_1 C_V{}^2 + m_0 C_V \gamma_1^+ - m_0 C_{ss} \gamma_1^- \right] - D_I C_I m_0 \left[\bar{\gamma}_0 + \gamma_1^+ \right]$$

$$\frac{\partial m_2}{\partial t} = D_V \left[4\lambda_1 C_V{}^2 + m_0 C_V \gamma_2^+ - m_0 C_{ss} \gamma_2^- \right] - D_I C_I m_0 \left[\bar{\gamma}_0 + \gamma_2^+ - 2\gamma_1^+ \right] \qquad (16)$$

$$\vdots$$

$$\frac{\partial C_V}{\partial t} = -D_V \left[2\lambda_1 C_V{}^2 + m_0 C_V \gamma_1^+ - m_0 C_{ss} \gamma_1^- \right] + D_I C_I m_0 \bar{\gamma}_0$$

$$\frac{\partial C_I}{\partial t} = -D_I C_I m_0 \left[\bar{\gamma}_0 + \gamma_1^+ \right]$$

Since we want to develop the most computationally efficient model, we consider the possibility of representing the system in terms of its first two moments following the work of Gencer and Dunham [18]. To further simplify, we can assume that the kinetic precipitation rate λ_n is a weak function of the precipitate size, and can replace λ_n by a constant effective value λ^{eff} for all sizes. λ^{eff} can be found approximately from a weighted sum of λ_n as:

$$\lambda^{\text{eff}} = \frac{\sum_{n=2}^{\infty} \lambda_n f_n}{\sum_{n=2}^{\infty} f_n} \qquad (17)$$

This effectively reduces the number of summations involved and thus our system reduces to:

$$\frac{\partial m_0}{\partial t} = I_1 = D\lambda_1 \left(C_V^2 - m_0 C_{ss} \gamma_0 \right) - D_I \lambda_1 C_I m_0 \bar{\gamma}_0$$

$$\frac{\partial m_1}{\partial t} = 2I_1 + D\lambda^{\text{eff}} m_0 \left(C_V - C_{ss} \gamma_1 \right) - D_I C_I m_0 \left(\lambda^{\text{eff}} - \bar{\gamma}_0 \lambda_1 \right) \qquad (18)$$

$$\frac{\partial C_V}{\partial t} = -\left[2I_1 + D\lambda^{\text{eff}} m_0 \left(C_V - C_{ss} \gamma_1 \right) + D_I \lambda_1 C_I m_0 \bar{\gamma}_0 \right]$$

$$\frac{\partial C_I}{\partial t} = -D_I C_I m_0 \left(\lambda^{\text{eff}} + \lambda_1 \bar{\gamma}_0 \right)$$

with

$$\gamma_0 = \hat{C}_1^* \hat{f}_2$$

$$\bar{\gamma}_0 = \hat{f}_2 = \gamma_0 / \hat{C}_1^* \qquad (19)$$

$$\gamma_1 = \sum_{n=2}^{\infty} \hat{C}_n^* \hat{f}_{n+1}$$

In order to solve this system of equations, we need to assume that it is possible to write the γ_i in terms of the moments for which we are solving, m_0 and m_1. Since the γ_i are functions of the normalized size distribution $\hat{f}_n$, they depend on m_0 and m_1 only through their ratio $\hat{m}_1 = m_1/m_0$, the average size. Thus we can write:

$$\gamma_0 = \gamma_0(\hat{m}_1)$$

$$\gamma_1 = \gamma_1(\hat{m}_1) \qquad (20)$$

To validate our assumption on the nature of f_n, it is possible to calculate the γ_i numerically and thus verify if γ_i are indeed uniquely dependent on $\hat{m}_1$. This approach was previously used by Hobler *et al.* for I aggregation.[25] The full discrete rate equation model was simulated at a single grid point. A large maximum size of 1000 was chosen to remove any errors due to pile-up at the largest size. The simulation
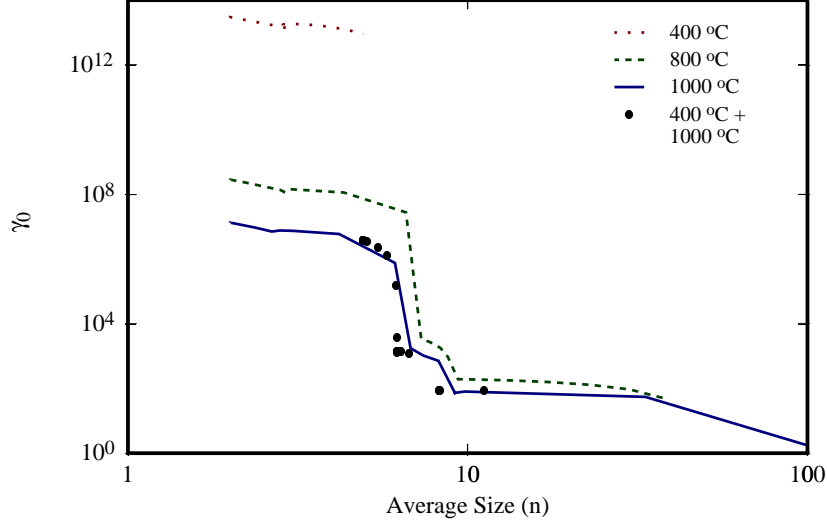
Fig. 9: γ_0 values extracted from simulations of the full system of rate equations for three different temperatures (400, 800, 1000°C). Also shown in the same plot is γ_0 value for a 1000°C anneal after a preanneal at 400°C. Note that the γ_0 is almost independent of its thermal history.

was run for different times to extract γ_i and $\hat{m}_1$. Figs. 9 and 10 show γ_i plotted against $\hat{m}_1$ extracted from the full model. It can be noted that γ_i satisfy the following limits as expected:[18]

$$
\begin{aligned}
\lim_{\hat{m}_1 \to 2} \gamma_0 &= \hat{C}_1^* \\
\lim_{\hat{m}_1 \to \infty} \gamma_0 &= 0 \\
\lim_{\hat{m}_1 \to 2} \gamma_1 &= 0 \\
\lim_{\hat{m}_1 \to \infty} \gamma_1 &= 1
\end{aligned}
\tag{21}
$$

For larger $\hat{m}_1$, γ_i are found to have only a weak dependence on temperature. Further, γ_i seem to be unique functions of $\hat{m}_1$ within reasonable errors. However to confirm this hypothesis it is necessary to be able to obtain the same γ_i irrespective of its thermal history. Figs. 9 and 10 include comparisons between single and two-step anneal. It was found that samples simulated at 1000°C with and without a 400°C preanneal gave very similar γ_i, giving credence to the possibility of using only the first two moments to model this system.

It is now possible to find analytic expressions to fit the obtained γ_i. For example, Figs. 11(a) and (b) show fits to the calculated γ_i. We can use the obtained γ_i in Eq. 18. We refer this model as the analytic kinetic precipitation model (AKPM). There are no other free parameters in this system. Note that C_{ss} can be taken as C_V^* and is not a fitting parameter. However, using the γ_i thus derived, we found the simulation to be numerically unstable due to the strong change in γ_i at small average sizes. Hence, a new set of γ_i were constructed neglecting small size effects. A kinetic barrier can be added to correct for the growth rate at small sizes. This is appropriate as kinetic factors are primarily significant at short times, and the large gamma values at small sizes inhibit the initial cluster formation and growth (see Eq. 18). Figs. 12(a) and (b) show such γ_i values. A barrier of 0.4 eV was added to the clustering reactions as a correction to include small size effects. This system was found to match closely both the experimental data and the full rate equation model. Fig. 13 illustrates this for anneals at 950 and 1000°C.
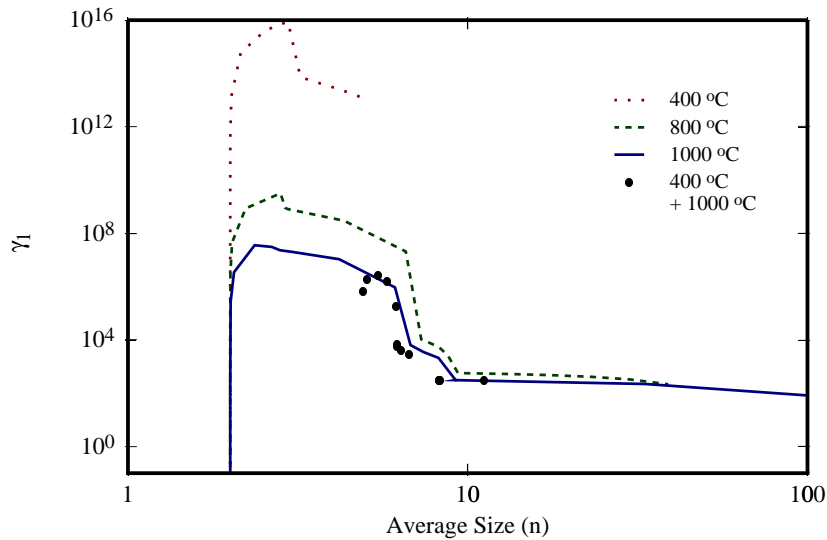
Fig. 10: γ_1 values extracted from simulations of the full system of rate equations for three different temperatures (400, 800, 1000°C). Also shown in the same plot is γ_1 value for a 1000°C anneal after a preanneal at 400°C. Note that the γ_1 is almost independent of its thermal history.

6. Summary

A set of discrete clusters are used to model vacancy cluster evolution after high energy ion-implantation in Si. The parameters for this system are from atomistic calculations. It was found that this system is able to predict the temperature, time and depth dependence of vacancy clusters seen in the experimental results. A procedure has been proposed to reduce this complex model into a simple two-moment model. The parameters for this two moment model are derived from the full rate equation model and are found to give good prediction to data. This efficient two-moment model can be easily incorporated into technology modeling tools and applied to model more complex situations.

7. Acknowledgments

[1]A. Bongiorno, L. Colombo, and T. Diaz de la Rubia, *Europhys. Lett.* **43**, 695 (1998).

[2]V. C. Venezia, D. J. Eaglesham, T. E. Haynes, A. Agarwal, D. C. Jacobson, H. J. Gossmann, and F. H. Baumann, *Appl. Phys. Lett.* **73**, 2980 (1998).

[3]J. Chen, S. Bharatan, and K.S. Jones, in **Defects and Diffusion in Silicon Processing**, Mater. Res. Soc. Meet., (1997).

[4]M.D. Giles, H.W. Kennel, P.A. Packan, and S. Yu, in **Defects and Diffusion in Silicon Processing**, Mater. Res. Soc. Proc., 253 (1997).

[5]D. J. Eaglesham, T. E. Haynes, H. J. Gossmann, D. C. Jacobson, P. A. Stolk, and J. M. Poate, *Appl. Phys. Lett.* **70**, 3281 (1997).

[6]R. A. Brown, O. Kononchuk, G. A. Rozgonyi, S. Koveshnikov, A. P. Knights, P. J. Simpson, and F. González, *Europhys. Lett.* **43**, 695 (1998).
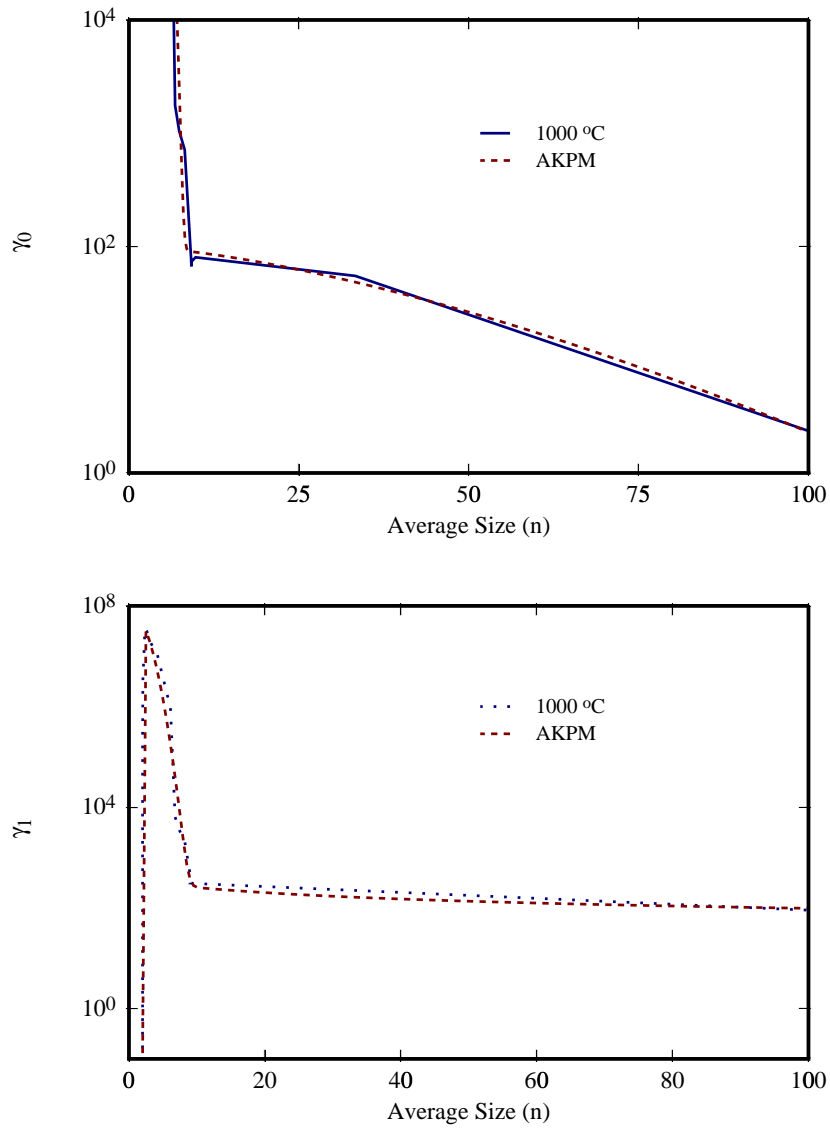
Fig. 11: Analytic fit to extracted (a) γ_0 and (b) γ_1 at 1000°C. Note the rapid change in γ_i at small sizes.
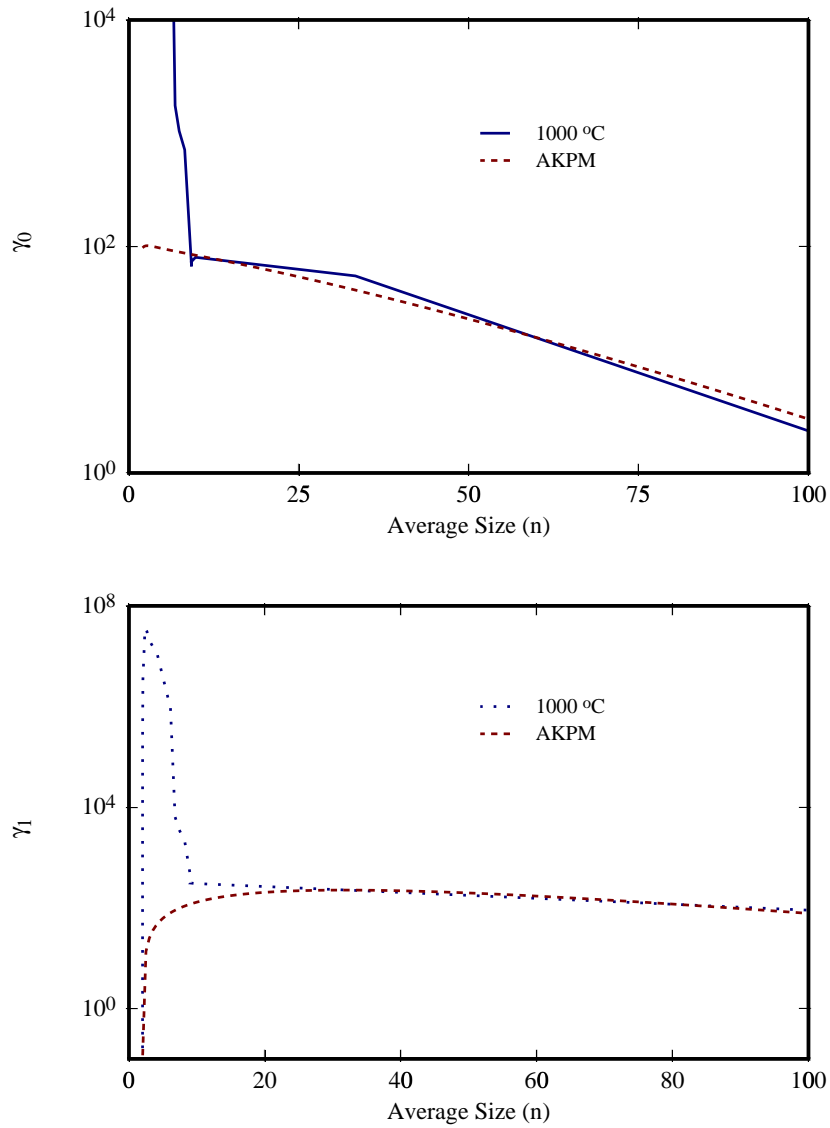
Fig. 12: Analytic fit to (a) γ_0 and (b) γ_1 neglecting the sharp change in γ_i during small sizes ($n < 10$).
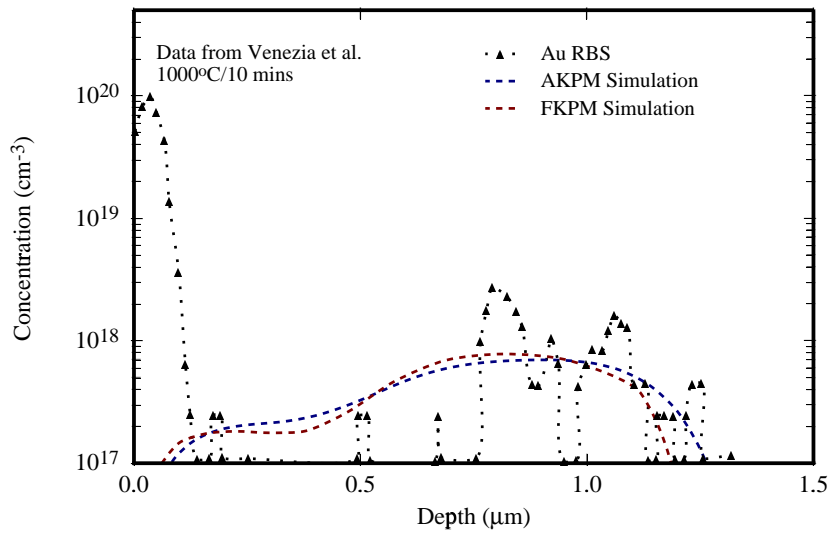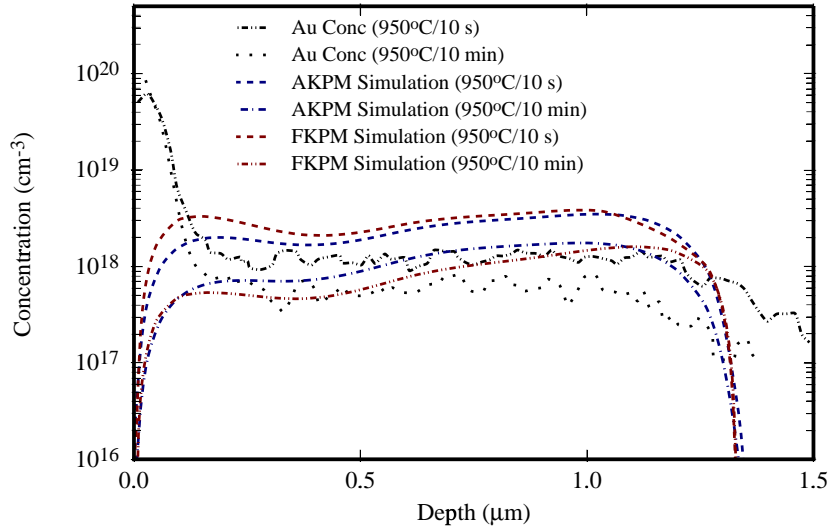
Fig. 13: Comparison of AKPM and full discrete cluster model at (a) 950°C and (b) 1000°C. Experimental Au concentration data is from Venezia *et al.* (Ref. 2).

[7]S. B. Herner, H. J. Gossmann, L. P. Pelaz, G. H. Gilmer, M. Jaraiz, and D. C. Jacobson, *J. Appl. Phys.* **83**, 6182 (1998).

[8]E. G. Roth, O.W. Holland, and A. Meldrum, in **Silicon Materials Science and Technology**, Electrochem. Meet. Proc., 938 (1998).

[9]A. Sultan, S. Banerjee, S. List, and V. McNeil, *J. Appl. Phys.* **83**, 8046 (1998).

[10]M. Jaraiz, G. H. Gilmer, J. M. Poate, and T. D. de la Rubia, *Appl. Phys. Lett.* **68**, 409 (1996).

[11]S. T. Dunham, *J. Electrochem. Soc.* **139**, 2628 (1992).

[12]S. Chakravarthi and S.T. Dunham, in **Defects and Diffusion in Silicon Processing**, Mater. Res. Soc. Proc., 47 (1997).

[13]M. Tang, L. Colombo, J. Zhu, and T. Diaz de la Rubia, *Phys. Rev. B* **55**, 14279 (1997).

[14]H. Bracht, N. A. Stolwijk, and H. Mehrer, *Phys. Rev. B* **52**, 16542 (1995).

[15]J.P. Biersack, *Nuc. Inst. and Meth. B* **19**, 32 (1986).

[16]A.H. Gencer and S.T. Dunham, *J. Appl. Phys.* **81**, 631 (1997).

[17]A.H. Gencer, S. Chakravarthi, I. Clejan, and S.T. Dunham, in **Defects and Diffusion in Silicon Processing**, Mater. Res. Soc. Proc., 359 (1997).

[18]A. H. Gencer, PhD thesis, Boston University (1999).

[19]A.H. Gencer and S.T. Dunham, in **Si Front-End Processing-Physics and Technology of Dopant-Defect Interactions**, Mater. Res. Soc. Meet., (1999).

[20]G.Z. Pan, K.N. Tu, and S. Prussin, *Appl. Phys. Lett.* **68**, 1654 (1996).

[21]D.J. Eaglesham, P.A. Stolk, H.J. Gossmann, and J.M. Poate, *Appl. Phys. Lett.* **65**, 2305 (1994).

[22]D.J. Eaglesham, P.A. Stolk, H.J. Gossmann, T.E. Haynes, and J.M. Poate, *Nuc. Inst. and Meth. B* **106**, 191 (1995).

[23]R. Kalyanaramana, T. E. Haynes, V. C. Venezia, D. C. Jacobson, H.-J. Gossmann, and C. S. Rafferty, *Appl. Phys. Lett.* **76**, 3379 (2000).

[24]I. Clejan and S.T. Dunham, *J. Appl. Phys.* **78**, 7327 (1995).

[25]G. Hobler and C.S. Rafferty, in **Si Front-End Processing—Physics and Technology of Dopant-Defect Interactions**, Mater. Res. Soc. Proc., 123 (1999).